chemosensors

MDPI

*Article*

# Highly Sensitive p-$SmFeO_3$/p-$YFeO_3$ Planar-Electrode Sensor for Detection of Volatile Organic Compounds

**Huiyang Liu [1], Denghui Zhu [1], Tingting Miao [1], Weikang Liu [1], Juan Chen [2], Bin Cheng [1], Hongwei Qin [1] and Jifan Hu [1,*]**

[1] State Key Laboratory for Crystal Materials, School of Physics, Shandong University, Jinan 250100, China
[2] The Fifth Research Institute of China Aerospace Science and Technology Corporation, Beijing 100000, China
* Correspondence: hujf@sdu.edu.cn; Tel.: +86-0531-88361560

**Abstract:** Nanocomposites of $SmFeO_3$/$YFeO_3$ (1:0, 0.8:0.2, 0.6:0.4, 0.4:0.6, 0.2:0.8, and 0:1) with different molar proportions were prepared by the sol–gel method. The material's properties were characterized by various test methods, such as scanning-electron microscopy (SEM) and X-ray photoelectron-diffraction spectrometry (XPS). The gas-sensing characteristics of the sensor were tested in darkness and under illumination using monochromatic light with various selected wavelengths. The test results show that the $SmFeO_3$/$YFeO_3$ sensor with the molar ratio of 0.4:0.6 had the highest gas response to volatile organic compound (VOC) gases and that the optimum operating temperature was lower (120 °C). The light illumination improved the sensor's sensitivity to gas. Under the 370-nanometer light illumination, the sensor's responses to 30 ppm of ethanol, acetone, and methanol gases were 163.59, 134.02, and 111.637, respectively, which were 1.35, 1.28, and 1.59 times higher, respectively, than those without light. The high gas sensitivity of the sensor was mainly due to the adsorption of oxygen on the material's surface and the formation of a p–p heterojunction. The $SmFeO_3$/$YFeO_3$ sensor, which can respond to different VOC gases, can be used to detect the safety of unknown environments and provide a timely warning of the presence of dangerous gases in working environments.

**Keywords:** heterojunction; gas sensor; light illumination; volatile organic compound; sensing characteristics; sensing mechanism



**Citation:** Liu, H.; Zhu, D.; Miao, T.; Liu, W.; Chen, J.; Cheng, B.; Qin, H.; Hu, J. Highly Sensitive p-$SmFeO_3$/p-$YFeO_3$ Planar-Electrode Sensor for Detection of Volatile Organic Compounds. *Chemosensors* **2023**, *11*, 187. https://doi.org/10.3390/chemosensors11030187

Academic Editor: Boris Lakard

Received: 19 February 2023
Revised: 7 March 2023
Accepted: 9 March 2023
Published: 10 March 2023



## 1. Introduction

As society develops, increasing attention is paid to the harmful effects of VOC to the human body and the environment. Ethanol, acetone, methanol, and formaldehyde are all volatile organic compound gases. The impact of these gases on the human body has a negative effect on the respiratory system, and can even cause cancer, threatening human life [1–3]. Therefore, the preparation of sensors that can effectively detect VOC gases has received extensive attention. Semiconductor materials [4–12] are the most common gas-sensing materials due to their excellent physical and chemical properties. The detection of harmful gases by the semiconductor detector was shown by the resistance change of the sensor. Semiconductors such as $WO_3$ [13], ZnO [14], and $LaFeO_3$ [15], have been widely investigated as sensor materials for detecting various gases. In semiconductor materials, perovskite-type oxides of $ABO_3$ have been widely studied [16–28]. There are many chemical elements to choose from for cations at the A and B positions in $ABO_3$. Compared with traditional oxide-gas-sensing materials, perovskite materials are more stable, so they are expected to exhibit unique advantages in gas sensors.

As typical p-type-semiconductor perovskite materials, $SmFeO_3$ nanomaterials have attracted wide attention, and have high sensitivity to various VOC gases [29–31]. However, pure $SmFeO_3$ has some disadvantages, such as its high operating temperature and low response value. There are many ways to improve the gas-sensing performance of

pure $SmFeO_3$ perovskite sensors, such as by doping it with a noble metal [32–36]. The combination of these materials can overcome the shortages of pure metal materials and produce sensor materials with higher performance levels. In recent years, increasing attention has been paid in research to materials with heterojunction interfaces. Li et al. prepared a Co-$Fe_2O_3$/$SmFeO_3$ p–n-heterojunction composite using the sol–gel method with molecular imprinting technology, and the sensor's response to 5 ppm of methanol gas was 19.7 at 155 °C [37]. Zakie et al. synthesized a $SmFeO_3$/ZnO nanocomposite by the thermal treatment method, and the $SmFeO_3$/ZnO nanocomposite's sensor had a response of 45 to 10 ppm acetone at 350 °C [38]. These previous studies proved that the construction of a heterojunction can improve the gas-sensing characteristics of sensors. However, it is still important to find sensor materials with lower operating temperatures, faster response speeds, and higher response value.

In this paper, we combined another $YFeO_3$ rare-earth perovskite nanomaterial with $SmFeO_3$ to prepare $SmFeO_3$/$YFeO_3$ (0.8:0.2, 0.6:0.4, 0.4:0.6, and 0.2:0.8) nanomaterials with a heterojunction interface and different molar ratios. The characteristics of the sensitivity of the sensor to VOC gases were studied in the dark and under multi-wavelength-light illumination. The test results show that the $SmFeO_3$/$YFeO_3$ composite sensor had a higher gas-sensing performance than the pure $SmFeO_3$ and $YFeO_3$ sensors, and the optimal operating temperature of the sensor was 120 °C. The multi-wavelength-light illumination improved the sensor's response to the VOC gases. In addition, we also discuss the gas-sensing response mechanism of the $SmFeO_3$/$YFeO_3$ sensor.

## 2. Materials and Methods

### *2.1. Preparation of Nanomaterials*

The $SmFeO_3$/$YFeO_3$ (e:f) nanomaterials with a heterojunction interface were prepared using the sol–gel method. In our previous research [39,40], we successfully prepared $SmFeO_3$ and $YFeO_3$ nanomaterials with different annealing temperatures (500–900 °C) using the sol–gel method. Previous studies proved that when the annealing temperature was 700 °C, $SmFeO_3$ and $YFeO_3$ nanomaterial sensors had the best gas-sensing properties. Consequently, we mixed the $SmFeO_3$ and $YFeO_3$ nanomaterials (700 °C) according to different molar ratios (0.8:0.2, 0.6:0.4, 0.4:0.6, and 0.2:0.8), and then ground and fully mixed them. The mixture was annealed at 700 °C for 3 h and then ground again. Finally, the $SmFeO_3$/$YFeO_3$ (e:f) nanomaterials with a heterojunction interface were obtained.

### *2.2. Materials Characterization*

Using X-ray diffraction (XRD; 40 KV, 40 mA, Bruker D8 Advanced, Bruker Group, Billerca, MA, USA) with CuKα radiation, we measured the structural characteristics of the nanopowders. The microscopic morphology of the sample was observed by scanning-electron microscopy (SEM). The elemental composition and valence state of the samples were observed with an X-ray photoelectron-diffraction spectrometer (XPS; Thermo Scientific Escalab 250Xi, Thermo Fisher Scientific, Inc., Waltham, MA, USA). The ultraviolet–visible (UV–Vis) absorption spectra of the powder samples were tested by a UV–Vis–NIR spectrometer (UV–Vis–NIR, Cary 5000, Agilent, Palo Alto, CA, USA).

### *2.3. Fabrication and Measurement of Gas Sensors*

The $SmFeO_3$/$YFeO_3$ (e:f) powder samples were mixed with a small amount of deionized water and ground into a paste. Next, they were coated on the 1.5 × 1-millimeter planar electrode to prepare the planar-electrode sensors. In our previous research [39,40], we used the same planar electrode. One side was the material coating surface, with two platinum electrodes (for measurement), and the other side was the heating layer, with two platinum electrodes (for heating). After the preparation, the sensor was placed on a 200 °C aging table and heated for 48 h to improve its stability.

We used the gas-sensitivity-test system produced by Zhengzhou Weisheng company (WS-30A, Weisheng Electronics Co., Ltd., Zhengzhou, China) to test the performance of the

fabricated gas sensor. The system reflects the characteristics of the gas sensor by measuring the voltage of the load resistance in series with the gas sensor. The sensor's response is defined as $S = R_g/R_a$, where $R_g$ and $R_a$ are the resistance of the sensor in target gas and in the air, respectively. The response time is the time it takes for the resistance to increase to 90% of the change. The recovery time is the time taken to reduce the sensor resistance to 10% of the change.

## 3. Results

### *3.1. Nanomaterial Characterization*

Figure 1 shows the XRD patterns of the $SmFeO_3/YFeO_3$ (e:f) nanomaterials. The XRD pattern provides the crystallinity information of the nanostructures of the powder materials. The $YFeO_3$ sample was a hexagonal lattice structure (PDF#48-0529) [41–45]. The peaks of the $YFeO_3$ in Figure 1 mainly correspond to the (100), (101), (102), (104), (110), (106), and (114) crystal planes. The $SmFeO_3$ sample had an orthogonal lattice structure (PDF#39-1490) [46–48], and the XRD diffraction peaks in the figure correspond to the (101), (111), (200), (121), (002), (210), (220), (022), (131), (202), (040), (212), (311), (321), (240), (042), (331), and (242) crystal planes. In the XRD spectra of the $SmFeO_3/YFeO_3$ nanocomposite materials with the ratios of 0.2:0.8, 0.4:0.6, 0.6:0.4, and 0.8:0.2, the characteristic peaks of the $SmFeO_3$ and $YFeO_3$ materials appeared at the same time, which signifies the coexistence of $SmFeO_3$ and $YFeO_3$ in the $SmFeO_3/YFeO_3$ composites. With the increase in the proportion of the $YFeO_3$ material, the relative intensity of the (102) diffraction peak of the $YFeO_3$ at 33.2° increased gradually, while the (121) diffraction peak of the $SmFeO_3$ at 32.7° decreased gradually.

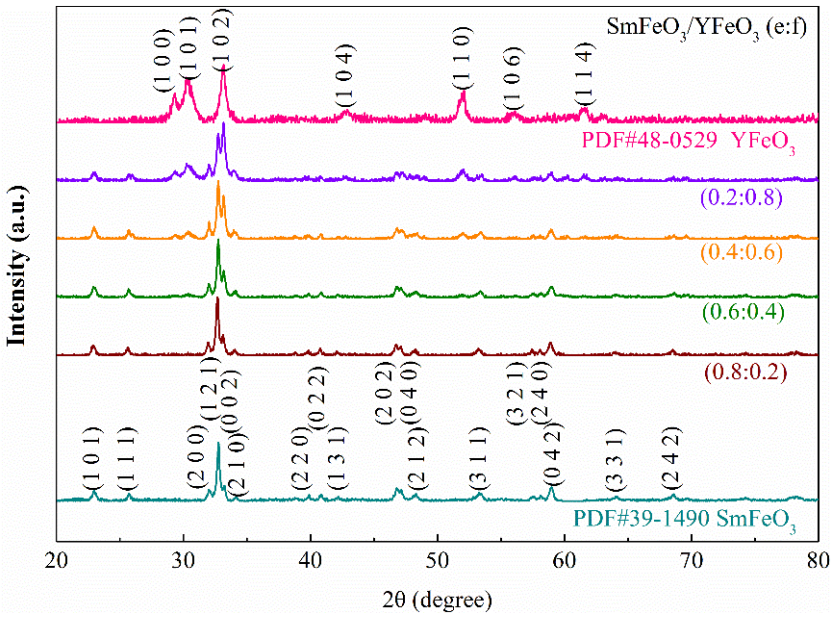


**Figure 1.** The X-ray diffraction patterns of $SmFeO_3/YFeO_3$ (e:f) powder nanomaterials.

Figure 2 shows the SEM spectra of the $SmFeO_3/YFeO_3$ (e:f) nanomaterials. The particle sizes were spherical below 100 nm, and some particles were elliptical after aggregation. When the mixing ratio of the two materials was different, the particle-size distribution of the materials also changed. The average particle sizes of the $SmFeO_3/YFeO_3$ (1:0, 0.8:0.2, 0.6:0.4, 0.4:0.6, 0.2:0.8, and 0:1) nanomaterials were 34.8, 42.1, 41.8, 38, 23.55, and 20.55 nm, respectively. The average particle size first increased and then decreased.

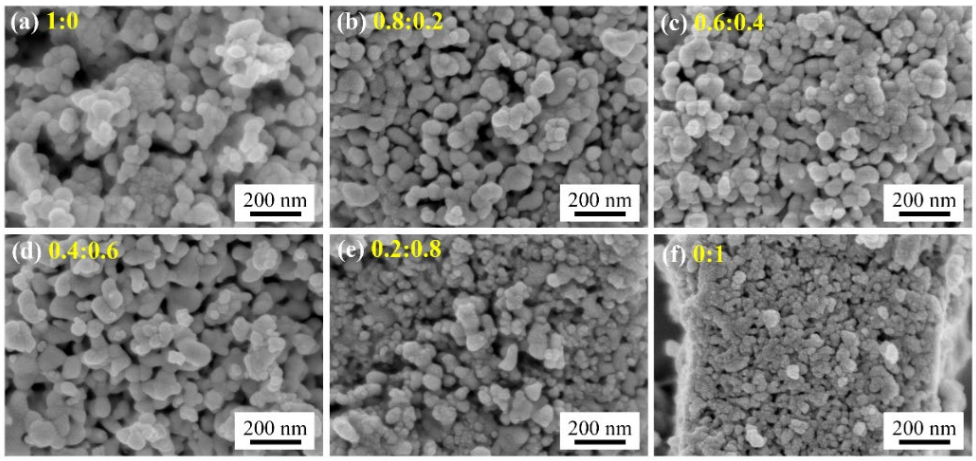


**Figure 2.** The SEM images of $SmFeO_3/YFeO_3$ (e:f) nanomaterials: (**a**) 1:0, (**b**) 0.8:0.2, (**c**) 0.6:0.4, (**d**) 0.4:0.6, (**e**) 0.2:0.8, and (**f**) 0:1.

Figure 3 shows the XPS spectra of the $SmFeO_3/YFeO_3$ (e:f) nanomaterials. The $SmFeO_3/YFeO_3$ nanomaterials mainly contained the characteristic peaks of Sm, Fe, Y, O, and C, without other impurity peaks, as shown in Figure 3a. It can be seen that the characteristic peaks of the Sm and Y elements changed significantly with the proportion of the materials. It is further proven that we successfully prepared $SmFeO_3/YFeO_3$ nanocomposite materials with different proportions. The Sm 3d spectra of the $SmFeO_3/YFeO_3$ were divided into $3d_{3/2}$ (1110.2 eV) and $3d_{5/2}$ (1083.2 eV) [46], as shown in Figure 3b. The peaks of Fe 2p at 724.5 ± 0.5 eV and 711 ± 0.2 eV corresponded to $2p_{1/2}$ and $2p_{3/2}$ [35], respectively, as shown in Figure 3c. Figure 3d shows the XPS spectra of the Y 3d, which were divided into two peaks of $3d_{3/2}$ (158.8 eV) and $3d_{5/2}$ (156.8 eV) [49].

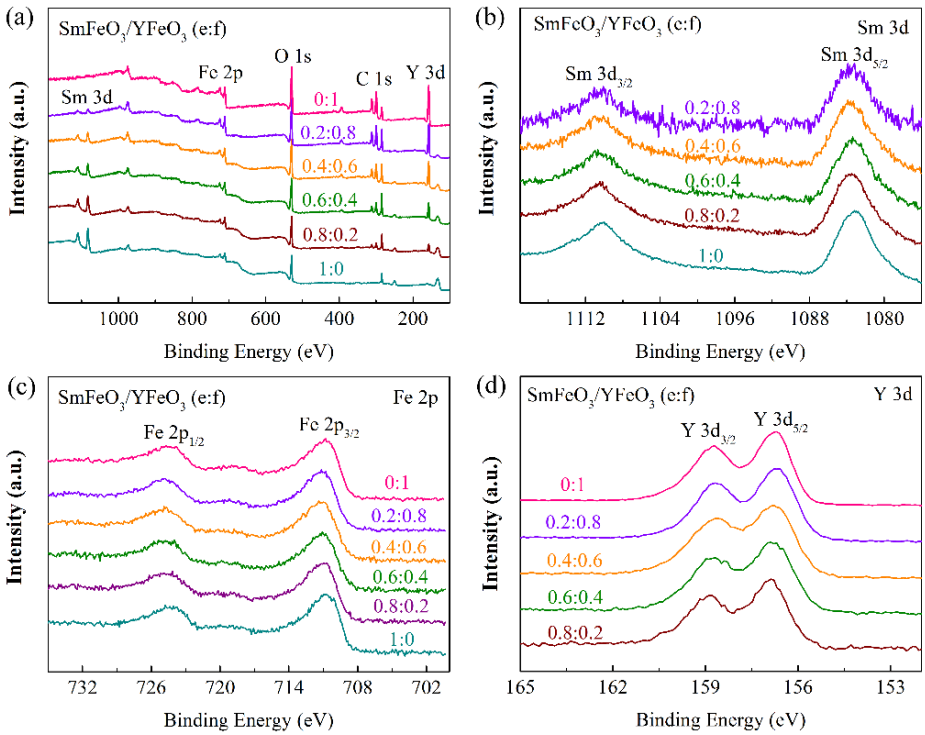


**Figure 3.** The XPS characterization of $SmFeO_3/YFeO_3$ (e:f) nanomaterials: (**a**) overall spectra, (**b**) Sm 3d, (**c**) Fe 2p, and (**d**) Y 3d.

Figure 4 shows the O 1s spectra analysis of the $SmFeO_3/YFeO_3$ nanomaterial. The XPS spectra of the O 1s were divided into three peaks, which correspond to three kinds of oxygen specification [50]. One corresponded to the lattice oxygen (529.4 ± 0.2 eV), one corresponded to the adsorbed oxygen (531.3 ± 0.5 eV), and one corresponded to the oxygen in the carbonate (532.5 ± 0.5 eV). The lattice oxygen and the oxygen in the carbonate did not react with the gas and had no effect on the carrier concentration on the material surface, so they did not affect the sensor performance. The adsorbed oxygen on the material surface reacted with the test gas, increasing the concentration of hole carriers, thus improving the response value of the sensor to the gas. The adsorbed oxygen contents on the surface of the $SmFeO_3/YFeO_3$ (e:f) nanomaterials were 28.19%, 31.34%, 37.58%, 39.94%, 32.15%, and 31.87% for the $SmFeO_3/YFeO_3$ nanomaterials with the proportions of 1:0, 0.8:0.2, 0.6:0.4, 0.4:0.6, 0.2:0.8, and 0:1, respectively. The changing trend is shown in Figure 5. The adsorbed oxygen content first increased and then decreased with the increase in the proportion of $YFeO_3$, and the adsorbed oxygen content of the $SmFeO_3/YFeO_3$ (0.4:0.6) material was the highest.

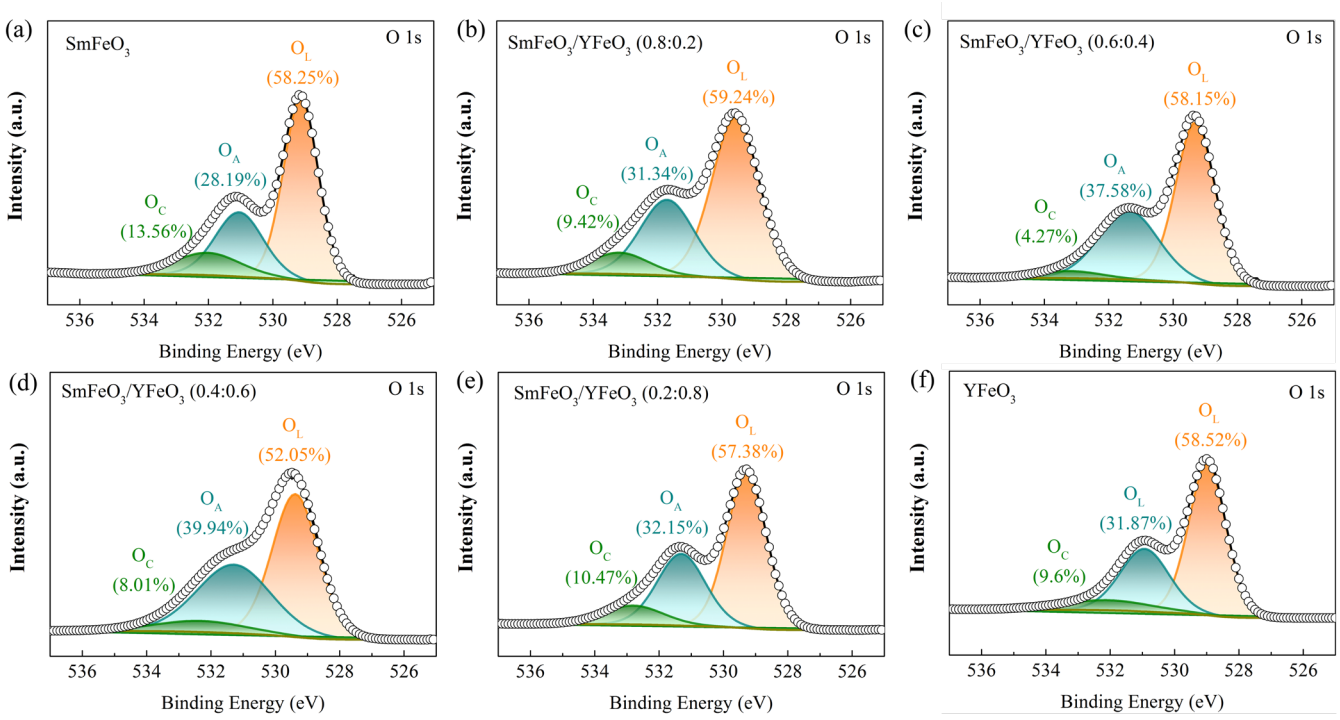


**Figure 4.** High-resolution XPS spectra of O 1s in $SmFeO_3/YFeO_3$ nanomaterials: (**a**) $SmFeO_3$, (**b**) 0.8:0.2, (**c**) 0.6:0.4, (**d**) 0.4:0.6, (**e**) 0.2:0.8, and (**f**) $YFeO_3$.

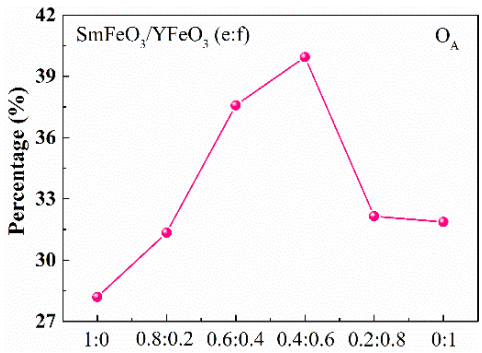


**Figure 5.** Change trend of the adsorbed oxygen content of $SmFeO_3/YFeO_3$ (e:f) nanomaterials.

### 3.2. Gas-Sensing Characteristics

In semiconductor gas sensors, the working temperature has a great influence on the gas-sensing characteristics. We tested the gas-sensitivity response of the $SmFeO_3/YFeO_3$ (1:0, 0.8:0.2, 0.6:0.4, 0.4:0.6, 0.2:0.8, and 0:1) sensors to ethanol, acetone, methanol, and formaldehyde gases in the dark at 100–150 °C, as shown in Figure 6. The response values of the $SmFeO_3/YFeO_3$ (e:f) sensors to the four gases had similar trends with temperature. With the increase in the working temperature, the response value first increased and then decreased, reaching the maximum value at 120 °C, with the exception of the optimal temperature of the $YFeO_3$ sensor, which was 110 °C. The reason for this trend was that, with the increase in the working temperature, the test gas overcame the energy barrier and encouraged the oxidation and reduction reaction on the material surface, so the sensor's response value increased. However, the high operating temperature caused the gas-desorption efficiency on the material surface to be greater than the adsorption efficiency, so the sensor's response value decreased. The sensor with the highest response value at 120 °C was $SmFeO_3/YFeO_3$ (0.4:0.6). The response values of the $SmFeO_3/YFeO_3$ (0.4:0.6) sensor to 30 ppm of ethanol, acetone, methanol, and formaldehyde were 120.76, 104.65, 70.43, and 9.21, respectively.

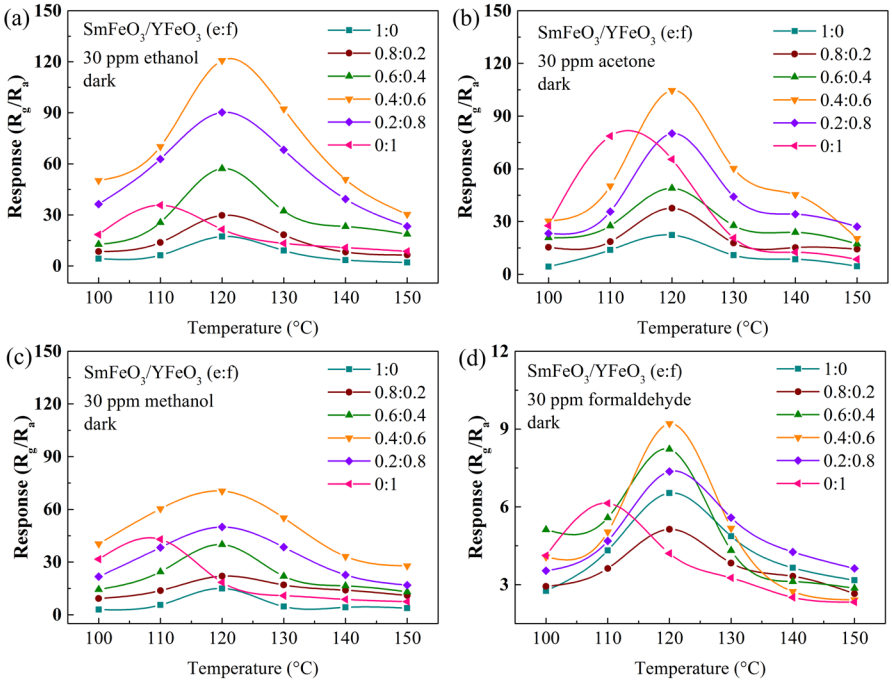


**Figure 6.** Response curves of the $SmFeO_3/YFeO_3$ (e:f) sensor to VOC gases in the dark with temperature: (**a**) ethanol, (**b**) acetone, (**c**) methanol, and (**d**) formaldehyde.

Figure 7 shows the curves of the $SmFeO_3/YFeO_3$ (0.4:0.6) sensor's response value to VOC gases with the operating temperature under multi-wavelength (470, 420, and 370 nm) light illumination. It can be seen that under the light illumination, the response value of the sensor first increased and then decreased with the change in the operating temperature at 100–150 °C. The optimum operating temperature was 120 °C. Compared with the darkness, we did not measure the change in the optimal operating temperature under light illumination. The temperature interval during the test was 10 °C due to the limitations of the equipment. The light-excitation energy within the wavelength range of the available light source was insufficient to cause visible temperature changes. At 120 °C, the $SmFeO_3/YFeO_3$ (0.4:0.6) sensor's response values to 30 ppm of ethanol, acetone, methanol, and formaldehyde under 370 nm of light illumination were 163.59, 134.02, 111.637, and 18.60, respectively, which were 1.35, 1.28, 1.59, and 2.02 times, respectively, those in the

dark. Therefore, it was confirmed that the multi-wavelength light illumination improved the response value of the sensor.

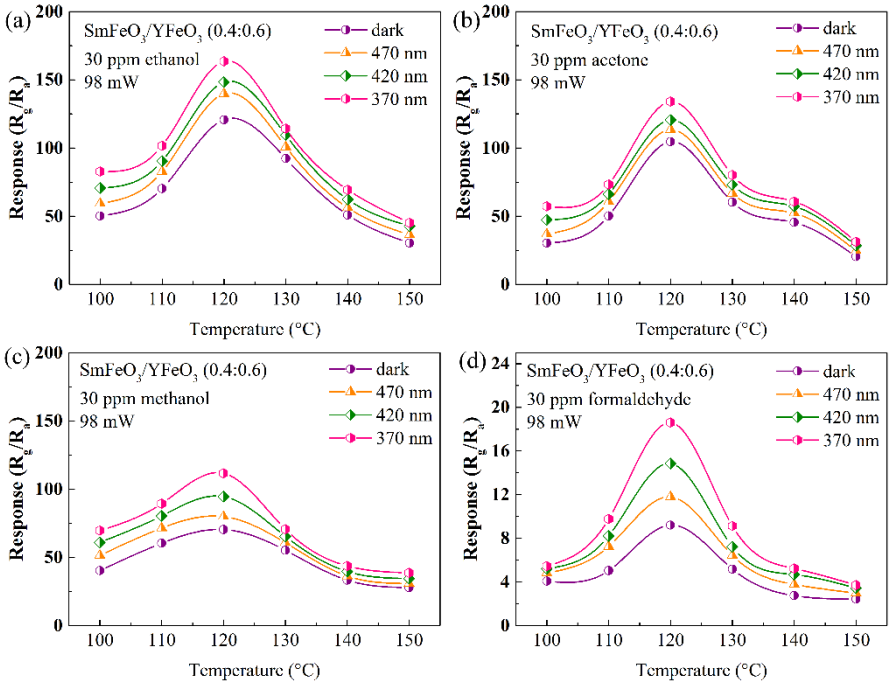


**Figure 7.** Response curves of the $SmFeO_3/YFeO_3$ (0.4:0.6) sensor to VOC gases under multi-wavelength light illumination with temperature: (**a**) ethanol, (**b**) acetone, (**c**) methanol, and (**d**) formaldehyde.

The repeatability of the sensor was an important parameter in the reliability of the sensor in use. A verified sensor would be expected achieve similar results for multiple tests in the same environment. The detection results of the $SmFeO_3/YFeO_3$ (0.4:0.6) sensor for three gases at 120 °C were repeated under 370 nm of light illumination, as shown in Figure 8. The $SmFeO_3/YFeO_3$ (0.4:0.6) sensor displayed good repeatability with VOC gases.

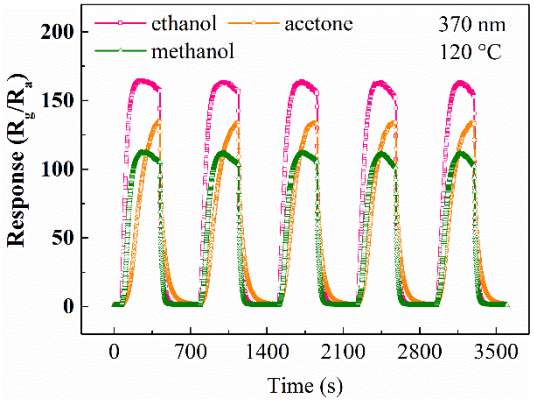


**Figure 8.** Repeatability test of sensitivity of the $SmFeO_3/YFeO_3$ (0.4:0.6) sensor to VOC gases in 5 cycles under 370 nm of light illumination.

We also tested the response/recovery time of the $SmFeO_3/YFeO_3$ (0.4:0.6) sensor under light illumination, as shown in Figure 9. Before the sensor contacted the target gas, the resistance was stable, and the log of R was about 6.55 Ω. After the target gas was introduced, the sensor's resistance increased, conforming to the characteristic of the p-type semiconductor material. However, due to the different gas characteristics, the response/recovery time of the sensor to the different gases varied greatly. Under the

370-nanometer light illumination, the response/recovery times of the $SmFeO_3/YFeO_3$ (0.4:0.6) sensor to 30 ppm of ethanol, acetone, methanol, and formaldehyde were 37/129 s, 166/228 s, 69/94 s, and 83/237 s, respectively. The fastest response of the sensor was to the ethanol gas, and the slowest response was to the acetone gas. The combination of the response value and the response/recovery time can be used as a parameter index to judge gas during the application of sensors.

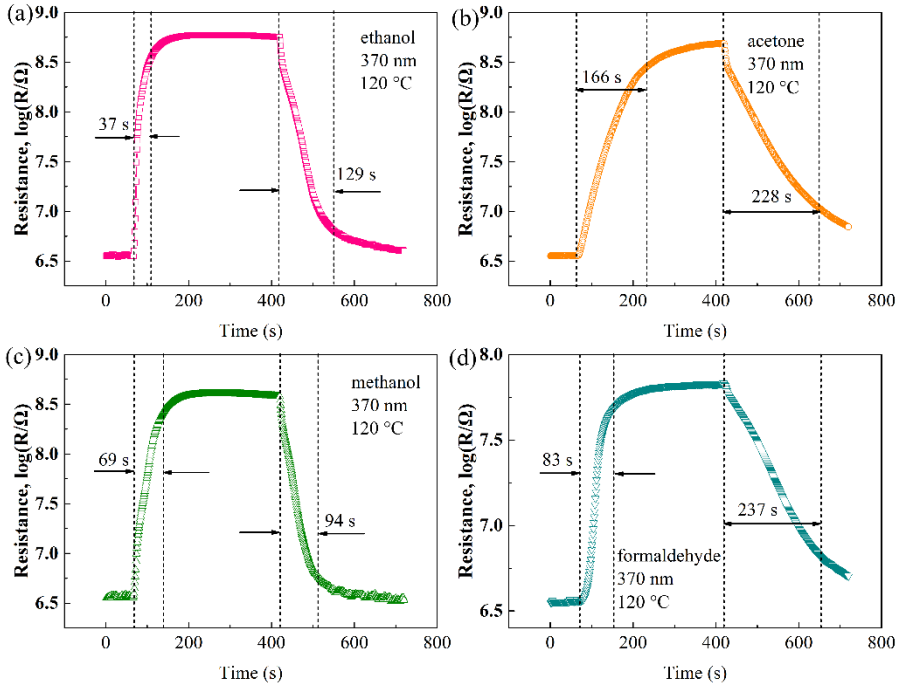


**Figure 9.** Response/recovery time of the $SmFeO_3/YFeO_3$ (0.4:0.6) sensor to VOC gases under 370 nm of light illumination: (**a**) ethanol, (**b**) acetone, (**c**) methanol, and (**d**) formaldehyde.

Figure 10 shows the dynamic-response curve and change curve of the $SmFeO_3/YFeO_3$ (0.4:0.6) sensor's response to VOC gases at 120 °C with the change in concentration. When the concentrations of the ethanol, acetone, and methanol gases increased from 10 ppm to 50 ppm, the response value of the $SmFeO_3/YFeO_3$ (0.4:0.6) sensor increased gradually. After several cycles, the resistance of the $SmFeO_3/YFeO_3$ (0.4:0.6) sensor recovered to a level close to that in the air, as shown in Figure 10a–c. As can be seen from Figure 10d, the $SmFeO_3/YFeO_3$ (0.4:0.6) sensor's response value increased with the gas concentration at 10–50 ppm. As shown in Figure 10e, we tested the linear relationship between the response value of the $SmFeO_3/YFeO_3$ (0.4:0.6) sensor and the gas concentration (0.5–10 ppm). The $SmFeO_3/YFeO_3$ (0.4:0.6) sensor demonstrated a good linear relationship with the three gases at low concentrations. The slopes of the linear relationship between the sensor and the concentrations of the three gases were 7.765, 5.126, and 2.833. According to the linear relationship, the detection limit of the sensor for the ethanol, acetone, and methanol gases can be calculated as 0.38, 0.42, and 0.67ppm, respectively. Therefore, the sensor has not only a high response value but also a low detection limit.

At an optimum operating temperature of 120 °C, the gas-sensing characteristics of the $SmFeO_3/YFeO_3$ (0.4:0.6) sensor under 370 nm of light illumination were tested at different humidity levels, as shown in Figure 11. Figure 11a shows that the $SmFeO_3/YFeO_3$ (0.4:0.6) sensor's dynamic-response curve to 30 ppm of the ethanol gas gradually decreased with the increase in humidity. When the humidity decreased from 30% RH to 80% RH, the response value of the sensor decreased by about 20%. Under different humidity conditions, the resistance of the $SmFeO_3/YFeO_3$ (0.4:0.6) sensor recovered to close to the initial value after the gas desorption. The variation curves of the $SmFeO_3/YFeO_3$ (0.4:0.6) sensor's response to the ethanol, acetone, and methanol gases with relative humidity are shown

in Figure 11b, and it can be seen that the response value decreased with the increase in relative humidity. The relative humidity in the air is high in summer, so the measurement results of the sensor were low during this season.

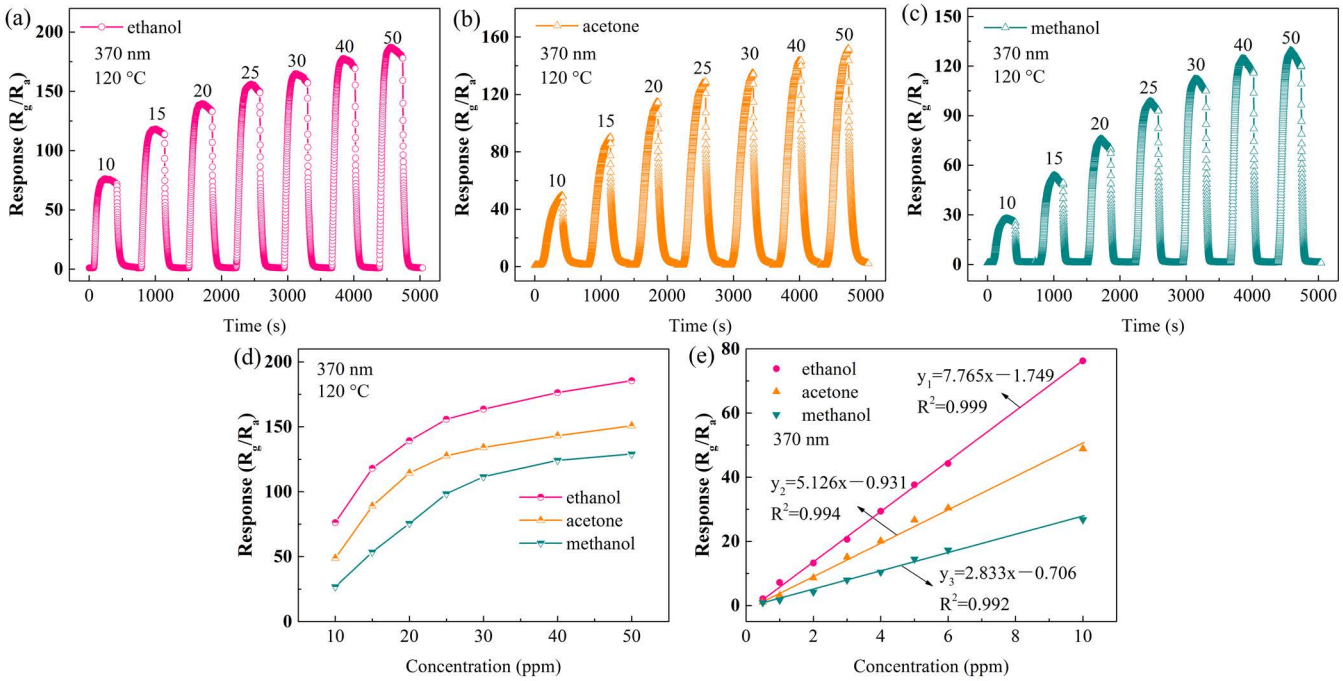


**Figure 10.** The dynamic-response curve of the $SmFeO_3/YFeO_3$ (0.4:0.6) sensor to (**a**) ethanol, (**b**) acetone, and (**c**) methanol gases with different gas concentrations; (**d**) change curves of the $SmFeO_3/YFeO_3$ (0.4:0.6) sensor's response with concentration at 120 °C; (**e**) the linear-fit curves of the gas responses for $SmFeO_3/YFeO_3$ (0.4:0.6) sensor.

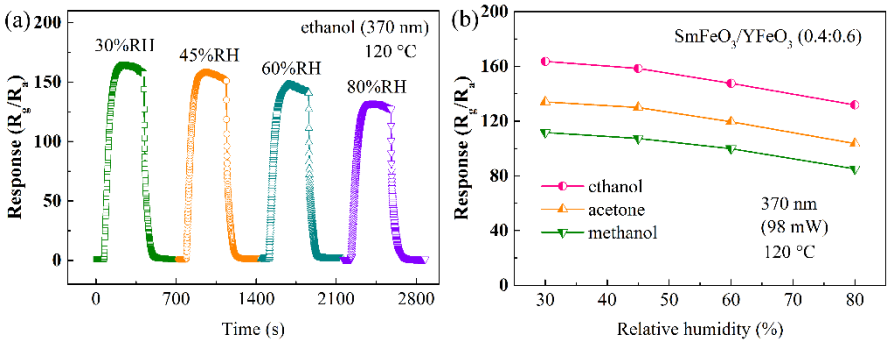


**Figure 11.** (**a**) Dynamic-response curve under different humidity levels of the $SmFeO_3/YFeO_3$ (0.4:0.6) sensor for ethanol gas; (**b**) variation curves with humidity of the $SmFeO_3/YFeO_3$ (0.4:0.6) sensor for VOC gases under 370 nm of light illumination.

The power parameters of the light sources were set by adjusting the corresponding voltage on the LED light-source device. Figure 12 shows the dynamic-response curves of the $SmFeO_3/YFeO_3$ (0.4:0.6) sensor to the VOC gases (ethanol, acetone, methanol, and formaldehyde) under multi-wavelength light illumination (with different optical powers) at 120 °C. Under the same wavelength of light illumination, the greater the optical power (30, 50, and 98 mW), the higher the response value of the $SmFeO_3/YFeO_3$ (0.4:0.6) sensor. When the optical power was the same, the shorter the wavelength of the light source (470, 420, and 370 nm), the higher the response value of the $SmFeO_3/YFeO_3$ (0.4:0.6) sensor.

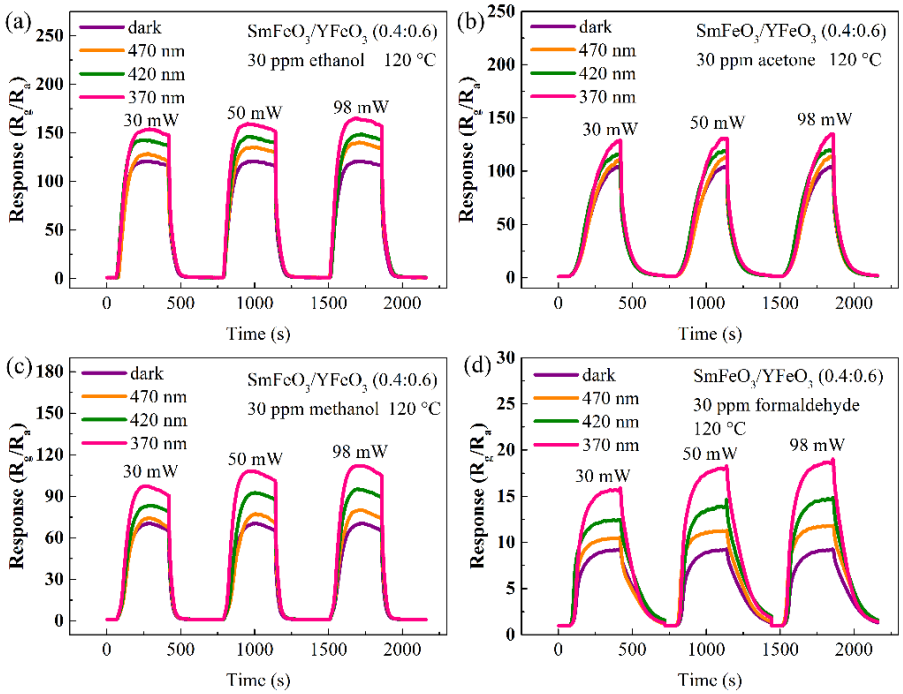


**Figure 12.** Dynamic-response curves under different optical powers of the $SmFeO_3/YFeO_3$ (0.4:0.6) sensor for VOC gases under multi-wavelength light illumination: (**a**) ethanol, (**b**) acetone, (**c**) methanol, and (**d**) formaldehyde.

Figure 13a shows the response histogram of the $SmFeO_3/YFeO_3$ (0.4:0.6) sensor to the VOC gases at 120 °C under 370 nm of light illumination. The response value of the sensor to 30 ppm ethanol was the highest. Although the sensor's response values to the acetone and methanol gases were lower than those for the ethanol, the response values were still high. Therefore, the $SmFeO_3/YFeO_3$ (0.4:0.6) sensor can detect various gases. Figure 13b shows the stability-test curves of the $SmFeO_3/YFeO_3$ (0.4:0.6) sensor for the VOC gases at 120 °C under 370 nm of light illumination over 35 days. The value of the $SmFeO_3/YFeO_3$ (0.4:0.6) sensor's response to the VOC gases changed little and had good stability.

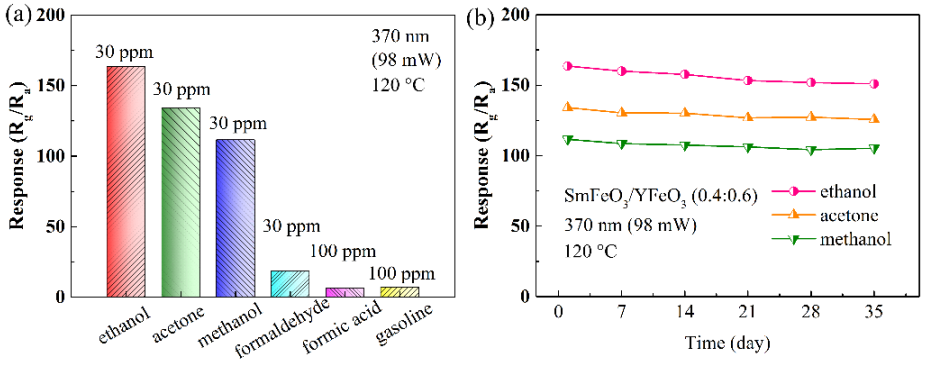


**Figure 13.** (**a**) Response histogram of the $SmFeO_3/YFeO_3$ (0.4:0.6) sensor for VOC gases at 120 °C; (**b**) stability curves of the $SmFeO_3/YFeO_3$ (0.4:0.6) sensor for VOC gases at 120 °C within 35 days.

Table 1 shows a comparison of the gas-sensing characteristics between the $SmFeO_3/YFeO_3$ (0.4:0.6) sensor and other sensors. It can be seen that the optimal operating temperature of the $SmFeO_3/YFeO_3$ (0.4:0.6) sensor was lower and the gas-response value was higher.

**Table 1.** Comparison of gas-sensing performance between $SmFeO_3/YFeO_3$ (0.4:0.6) sensor and other perovskite sensors.

| Materials | Gas | Tem. (°C) | Con. (ppm) | Res. | Refs. |
|---|---|---|---|---|---|
| $NdFeO_3$ | ethanol | 250 | 100 | 150 | [16] |
| $La_{0.98}Ba_{0.02}FeO_3$ | ethanol | 200 | 100 | 79.3 | [51] |
| Au-$LaFeO_3$ | ethanol | 200 | 100 | 44 | [52] |
| $SmFeO_3$ | acetone | 210 | 1 | 5.92 | [29] |
| Pd-$SmFeO_3$ | acetone | 220 | 1 | 10.73 | [32] |
| $SmFeO_3$/ZnO | acetone | 350 | 10 | 45 | [38] |
| $YFeO_3$ | acetone | 110 | 30 | 128.1 | [40] |
| $DyFeO_3$ | acetone | 190 | 2 | 3.81 | [53] |
| $PrFeO_3$ | acetone | 180 | 10 | 6 | [54] |
| Sm-$PrFeO_3$ | acetone | 270 | 50 | 44.94 | [55] |
| Co-$Fe_2O_3/SmFeO_3$ | methanol | 155 | 5 | 19.7 | [37] |
| $SmFeO_3$ | methanol | 120 | 30 | 26.41 | [39] |
| $SmFeO_3/YFeO_3$ | ethanol | 120 | 30 | 163.593 | this work |
| $SmFeO_3/YFeO_3$ | acetone | 120 | 30 | 134.023 | this work |
| $SmFeO_3/YFeO_3$ | methanol | 120 | 30 | 111.637 | this work |

This kind of planar-electrode sensor has a small size, low optimal working temperature, high response value, and good stability, and detects various VOC gases. In the future, it will be possible to use them in portable or wearable gas sensors, which can detect the environment and warn users about the occurrence of dangerous gases in a timely manner.

### *3.3. Mechanism Discussion*

We studied the light-absorption ability of $SmFeO_3$, $YFeO_3$, and $SmFeO_3/YFeO_3$ composite materials with different molar-mass ratios by UV–visible absorption spectroscopy, as shown in Figure 14a. As demonstrated in to Figure 14a, we obtained the $(ahv)^2$–$(hv)$ curves of the $SmFeO_3$, and $YFeO_3$ samples, which are shown in Figure 14b. After the calculation, the band energies of the $SmFeO_3$ and $YFeO_3$ materials were 2.009 and 1.837 eV, respectively. The calculation formula is as follows:

$$ahv = \mathrm{A}(hv - E_g)^{1/2} \quad (1)$$

where A is a constant, $hv$ is the photon energy, $E_g$ is the band-gap energy of the material, and $a$ is the absorbance.

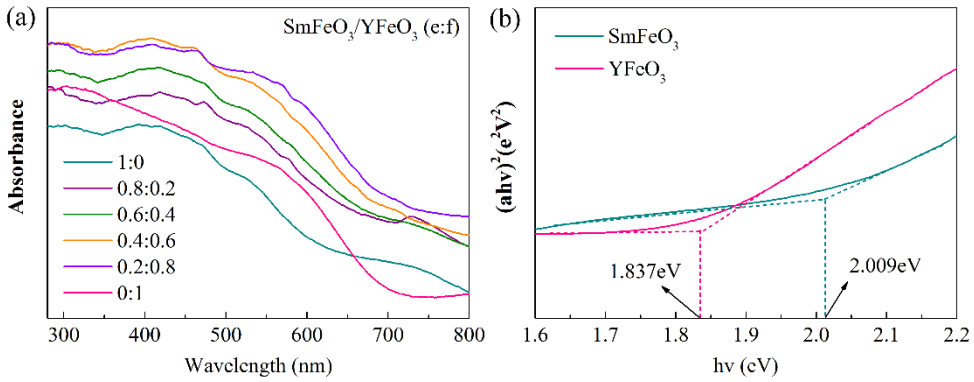


**Figure 14.** (**a**) The UV–visible absorption spectrum of $SmFeO_3/YFeO_3$ (e:f) powder samples; (**b**) the $(ahv)^2$–$(hv)$ curves of $SmFeO_3$ and $YFeO_3$ powder samples.

The photon energies of the light sources with the wavelengths of 470, 420, and 370 nm were 2.638, 2.952, and 3.351 eV, respectively. The photon energies of the light sources with different wavelengths were higher than the band energies of the $SmFeO_3$, $YFeO_3$, and nanomaterials with heterogeneous interfaces. Therefore, the light illumination caused the electronic transition on the material surface. The electronic transit to a higher energy level

improved the conductivity and reduced the resistance. Photoexcitation produces photo-generated electrons and holes, which can react with oxygen to produce more adsorbed oxygen ions, so the sensor reacts with more gases to improve its performance. Therefore, the light illumination improved the response of the $SmFeO_3/YFeO_3$ sensor due to the photoelectric effect.

The gas-sensing mechanism of the $SmFeO_3/YFeO_3$ (e:f) sensor under light illumination can be explained by the depletion layer and p–p heterojunction. In the $SmFeO_3/YFeO_3$ (e:f) nanomaterials, a p–p-heterojunction interface formed between the $SmFeO_3$ and $YFeO_3$ materials. The charge transfer led to a change in the barrier height. The p–p heterojunctions on the $SmFeO_3/YFeO_3$ interface acted as tunable resistors, resulting in differences in the sensor's resistance at different temperatures.

$$O_{2\,(gas)} \rightarrow O_{2\,(ads)} \quad (2)$$

$$O_{2\,(ads)} + e^- \rightarrow O_2{}^-{}_{(ads)} \quad (3)$$

$$O_2{}^-{}_{(ads)} + e^{\rightarrow} \rightarrow 2O^-{}_{(ads)} \quad (4)$$

$$C_2H_5OH_{\,(gas)} + 6O^-{}_{(ads)} \rightarrow 2CO_2 + 3H_2O + 6e^- \quad (5)$$

$$CH_3COCH_{3\,(gas)} + 8O^-{}_{(ads)} \rightarrow 3CO_2 + 3H_2O + 8e^- \quad (6)$$

$$CH_3OH_{\,(gas)} + 3O^-{}_{(ads)} \rightarrow CO_2 + 2H_2O + 3e^- \quad (7)$$

The $SmFeO_3$ and $YFeO_3$ materials are p-type semiconductors. After the contact between the two semiconductors, since the Fermi energy level of the $SmFeO_3$ was higher than that of the $YFeO_3$, the electrons flowed from the conduction band of the $SmFeO_3$ to the conduction band of the $YFeO_3$ material, resulting in the formation of energy-band bending [56–58] and a depletion layer, until the Fermi energy level reached the equilibrium state, as shown in Figure 15a. Under the light illumination, photo-generated electrons and holes were generated in the p–p heterojunction. At the same time, the built-in electric field generated between the heterojunctions inhibited the recombination of photo-generated electron–hole pairs. Therefore, there were more photo-generated electrons and holes on the surface of the material, which were able to react with oxygen to generate more adsorbed oxygen ions.

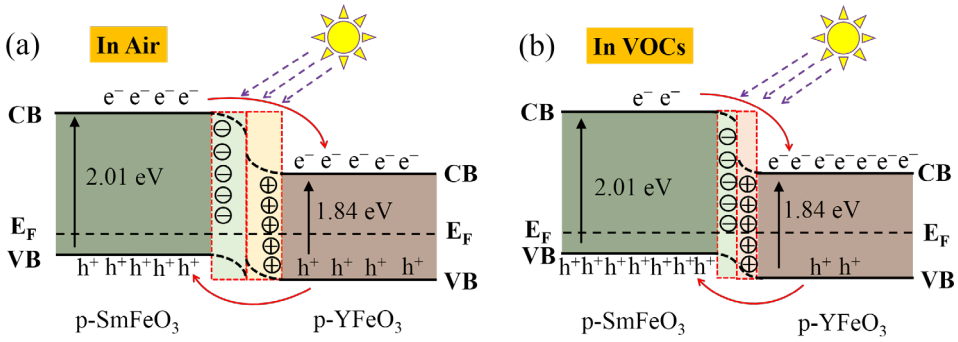


**Figure 15.** Schematic diagram of the energy band of the $SmFeO_3/YFeO_3$ composite material (**a**) in air and (**b**) VOC gases.

When the $SmFeO_3/YFeO_3$ nanomaterials were exposed to air, the oxygen molecules in the air made full contact with the materials' surfaces, capturing electrons in the materials' conduction bands to form oxygen ions, as shown in Formulas (2)–(4). Due to the presence of the electron-depletion layer, the sensor's resistance in the air was relatively low.

When the $SmFeO_3/YFeO_3$ sensors were in contact with the VOC gases, the gas molecules reacted with the oxygen ions and released electrons, as shown in Formulas (5)–(7). The electrons combated the holes in the materials, and the presence of electron–hole pairs

reduced the hole density in the nanocomposites and broke the dynamic-carrier balance between the $SmFeO_3$ and $YFeO_3$ materials. The hole transfer of the $SmFeO_3$ and $YFeO_3$ further reduced the thickness of the electron-depletion layer on the $SmFeO_3$ surface, so the resistance of the $SmFeO_3/YFeO_3$ sensor increased, as shown in Figure 15b. The dynamic-response curves of the resistance (Figure 9) of the $SmFeO_3/YFeO_3$ sensor to the VOC gases show that the sensor's resistance increased after its contact with the VOC gases, confirming the reliability of the sensing mechanism above.

## 4. Conclusions

In this study, $SmFeO_3/YFeO_3$ (e:f) nanocomposite materials with different proportions were prepared using the sol–gel method. A planar electrode measuring 1.5 × 1 mm was used to prepare the small-size planar-electrode sensor. The optimal working temperature of the $SmFeO_3/YFeO_3$ (e:f) planar-electrode sensor was 120 °C. Additionally, multi-wavelength light illumination improved the gas sensitivity of the sensor. Under the 370-nanometer light illumination, the values of the responses of the $SmFeO_3/YFeO_3$ (0.4:0.6) sensor to 30 ppm of the ethanol, acetone, methanol, and formaldehyde gases were 163.59, 134.02, 111.637, and 18.60, respectively, which were 1.35, 1.28, 1.59, and 2.02 times, respectively, those found in the dark. In addition, the gas-sensing mechanism of the sensor was explained by analyzing the p–p heterojunction. This planar-electrode sensor, with its small size, low operating temperature, and high gas-sensitivity-response value, has major potential for future use a portable gas sensor to detect VOC gases and warn users about potential dangers in unknown environments.

**Author Contributions:** Conceptualization, H.L., D.Z. and T.M.; methodology, H.L., W.L., J.C., B.C. and H.Q.; software, H.L., W.L. and J.C.; validation, T.M. and W.L.; formal analysis, D.Z.; investigation, H.L. and D.Z.; resources, T.M., W.L. and J.C.; data curation, H.L.; writing—original draft preparation, H.L.; writing—review and editing, H.L., J.H., J.C., B.C. and H.Q.; visualization, W.L.; supervision, J.H.; project administration, J.H.; funding acquisition, B.C., H.Q. and J.H. All authors have read and agreed to the published version of the manuscript.

**Funding:** This research was funded by the National Natural Science Foundation of China, grant numbers 51772174 (Jifan Hu), 51472145 (Hongwei Qin), and 11904204 (Bin Cheng).

**Institutional Review Board Statement:** Not applicable.

**Informed Consent Statement:** Not applicable.

**Data Availability Statement:** Not applicable.

**Acknowledgments:** This work was supported by the National Natural Science Foundation of China (grant numbers: 51772174, 51472145, and 11904204).

**Conflicts of Interest:** The authors declare no conflict of interest.

## References

1. Boots, A.W.; van Berkel, J.J.; Dallinga, J.W.; Smolinska, A.; Wouters, E.F.; van Schooten, F.J. The versatile use of exhaled volatile organic compounds in human health and disease. *J. Breath. Res.* **2012**, *6*, 027108. [CrossRef]
2. Park, A.S.; Ritz, B.; Ling, C.; Cockburn, M.; Heck, J.E. Exposure to ambient dichloromethane in pregnancy and infancy from industrial sources and childhood cancers in California. *Int. J. Hyg. Environ. Health* **2017**, *220*, 1133–1140. [CrossRef]
3. Int Panis, L.; de Geus, B.; Vandenbulcke, G.; Willems, H.; Degraeuwe, B.; Bleux, N.; Mishra, V.; Thomas, I.; Meeusen, R. Exposure to particulate matter in traffic: A comparison of cyclists and car passengers. *Atmos. Environ.* **2010**, *44*, 2263–2270. [CrossRef]
4. Jiang, Q.; Guo, X.; Wang, C.; Jia, L.; Zhao, Z.; Yang, R.; Wang, P.; Deng, Q. Polyvinylpyrrolidone-mediated $Co_3O_4$ microspheres assembled in size-tunable submicron spheres with porous core-shell structure for high-performance gases sensing. *J. Alloys Compd.* **2023**, *935*, 167976. [CrossRef]
5. Jin, Z.; Wang, C.; Wu, L.; Liu, H.; Shi, F.; Zhao, J.; Liu, F.; Fu, K.; Wang, F.; Wang, Z.; et al. Construction of Pt/Ce-$In_2O_3$ hierarchical microspheres for superior triethylamine detection at low temperature. *Colloids Surf. A* **2023**, *659*, 130738. [CrossRef]
6. Sun, B.; Shi, G.; Tang, Z.; Zhang, P.; Guo, Y.; Zhu, S.; Liu, J. Rapid gas-sensing detection of carbon disulfide by a CdS/SnS nanocomposite-based cataluminescence sensor. *Chemosensors* **2023**, *11*, 10. [CrossRef]
7. Liu, M.; Xue, L.; Feng, Q.; Wang, Y.; Liu, J.; Zhang, S.; Hu, W. Facile preparation of $Co_3O_4$ hollow dodecahedron with superior peroxidase-like activity for selective detection of cholesterol. *Chemosensors* **2023**, *11*, 27. [CrossRef]

8. Cui, X.; Lu, Z.; Wang, Z.; Zeng, W.; Zhou, Q. Highly sensitive SF6 decomposition byproducts sensing platform based on CuO/ZnO heterojunction nanofibers. *Chemosensors* **2023**, *11*, 58. [CrossRef]
9. Torai, S.; Ueda, T.; Kamada, K.; Hyodo, T.; Shimizu, Y. Effects of addition of $Cu_xO$ to porous $SnO_2$ microspheres prepared by ultrasonic spray pyrolysis on sensing properties to volatile organic compounds. *Chemosensors* **2023**, *11*, 59. [CrossRef]
10. Li, J.; Jin, Z.; Chao, Y.; Wang, A.; Wang, D.; Chen, S.; Qian, Q. Synthesis of graphene-oxide-decorated porous ZnO nanosheet composites and their gas sensing properties. *Chemosensors* **2023**, *11*, 65. [CrossRef]
11. Ur Rahman, Z.; Shah, U.; Alam, A.; Shah, Z.; Shaheen, K.; Bahadar Khan, S.; Ali Khan, S. Photocatalytic degradation of cefixime using CuO-NiO nanocomposite photocatalyst. *Inorg. Chem. Commun.* **2023**, *148*, 110312. [CrossRef]
12. Chen, Y.; Qin, H.; Cao, Y.; Zhang, H.; Hu, J. Acetone sensing properties and mechanism of $SnO_2$ thick-films. *Sensors* **2018**, *18*, 3425. [CrossRef] [PubMed]
13. Li, J.; Wu, J.; Yu, Y. DFT exploration of sensor performances of two-dimensional $WO_3$ to ten small gases in terms of work function and band gap changes and I-V responses. *Appl. Surf. Sci.* **2021**, *546*, 149104. [CrossRef]
14. Castello Lux, K.; Fajerwerg, K.; Hot, J.; Ringot, E.; Bertron, A.; Collière, V.; Kahn, M.L.; Loridant, S.; Coppel, Y.; Fau, P. Nanostructuration of $WO_3$ nanoleaves by localized hydrolysis of an organometallic Zn precursor: Application to photocatalytic $NO_2$ abatement. *Nanomaterials* **2022**, *12*, 4360. [CrossRef] [PubMed]
15. Chumakova, V.; Marikutsa, A.; Platonov, V.; Khmelevsky, N.; Rumyantseva, M. Distinct roles of additives in the improved sensitivity to CO of Ag- and Pd-modified nanosized $LaFeO_3$. *Chemosensors* **2023**, *11*, 60. [CrossRef]
16. Sheng, H.; Ma, S.; Han, T.; Yun, P.; Yang, T.; Ren, J. A highly sensitivity and anti-humidity gas sensor for ethanol detection with $NdFeO_3$ nano-coral granules. *Vacuum* **2022**, *195*, 110642. [CrossRef]
17. Rajaitha, P.M.; Hajra, S.; Padhan, A.M.; Panda, S.; Sahu, M.; Kim, H.J. An electrochemical sensor based on multiferroic $NdFeO_3$ particles modified electrode for the detection of $H_2O_2$. *J. Alloys Compd.* **2022**, *915*, 165402. [CrossRef]
18. Zhang, H.; Xiao, J.; Chen, J.; Zhang, L.; Zhang, Y.; Jin, P. Au modified $PrFeO_3$ with hollow tubular structure can be efficient sensing material for $H_2S$ detection. *Front. Bioeng. Biotechnol.* **2022**, *10*, 969870. [CrossRef]
19. Cai, Z.; Park, S. A superior sensor consisting of porous, Pd nanoparticle–decorated $SnO_2$ nanotubes for the detection of ppb-level hydrogen gas. *J. Alloys Compd.* **2022**, *907*, 164459. [CrossRef]
20. Bhardwaj, R.; Hazra, A. Pd functionalized $SrTiO_3$ hollow spheres for humidity-tolerant ethanol sensing. *Sens. Actuators B* **2022**, *372*, 132615. [CrossRef]
21. Yin, Y.; Shen, Y.; Zhao, S.; Bai, J.; Qi, Y.; Han, C.; Wei, D. Effect of noble metal elements on ethanol sensing properties of $ZnSnO_3$ nanocubes. *J. Alloys Compd.* **2021**, *887*, 161409. [CrossRef]
22. Han, T.; Ma, S.; Xu, X.; Cao, P.; Liu, W.; Xu, X.; Pei, S. Electrospinning synthesis, crystal structure, and ethylene glycol sensing properties of orthorhombic $SmBO_3$ (B. = Fe, Co) perovskites. *J. Alloys Compd.* **2021**, *876*, 160211. [CrossRef]
23. Yang, T.T.; Ma, S.Y.; Cao, P.F.; Xu, X.L.; Wang, L.; Pei, S.T.; Han, T.; Xu, X.H.; Yun, P.D.; Sheng, H. Synthesis and characterization of $ErFeO_3$ nanoparticles by a hydrothermal method for isopropanol sensing properties. *Vacuum* **2021**, *185*, 110005. [CrossRef]
24. Meng, F.; Hu, J.; Liu, C.; Tan, Y.; Zhang, Y. Highly sensitive and low detection limit of acetone gas sensor based on porous $YbFeO_3$ nanocrystallines. *Chem. Phys. Lett.* **2021**, *780*, 138925. [CrossRef]
25. Aranthady, C.; Jangid, T.; Gupta, K.; Mishra, A.K.; Kaushik, S.D.; Siruguri, V.; Rao, G.M.; Shanbhag, G.V.; Sundaram, N.G. Selective $SO_2$ detection at low concentration by Ca substituted $LaFeO_3$ chemiresistive gas sensor: A comparative study of $LaFeO_3$ pellet vs thin film. *Sens. Actuators B* **2021**, *329*, 129211. [CrossRef]
26. Chen, Y.; Wang, D.; Qin, H.; Zhang, H.; Zhang, Z.; Zhou, G.; Gao, C.; Hu, J. $CO_2$ sensing properties and mechanism of $PrFeO_3$ and $NdFeO_3$ thick film sensor. *J. Rare Earth* **2019**, *37*, 80–87. [CrossRef]
27. Zhang, H.; Qin, H.; Cheng, B.; Cao, Y.; Chen, Y.; Xie, J.; Liu, W.; Gao, C.; Zhou, G.; Hu, J. Pd:$LaFe_{0.9}Mg_{0.1}O_3$: Planar type acetone sensor with high sensitivity. *Mater. Sci. Semicond. Process.* **2019**, *96*, 91–98. [CrossRef]
28. Zhang, P.; Qin, H.; Zhang, H.; Lv, W.; Hu, J. $CO_2$ gas sensors based on $Yb_{1-x}Ca_xFeO_3$ nanocrystalline powders. *J. Rare Earth* **2017**, *35*, 602–609. [CrossRef]
29. Zhang, H.; Xiao, J.; Wang, Y.; Zhang, L.; Zhao, G.; Yang, H.; Wang, H. A portable acetone detector based on $SmFeO_3$ can pre-diagnose diabetes through breath analysis. *J. Alloys Compd.* **2022**, *922*, 166160. [CrossRef]
30. Han, T.; Ma, S.Y.; Xu, X.L.; Xu, X.H.; Pei, S.T.; Tie, Y.; Cao, P.F.; Liu, W.W.; Wang, B.J.; Zhang, R.; et al. Rough $SmFeO_3$ nanofibers as an optimization ethylene glycol gas sensor prepared by electrospinning. *Mater. Lett.* **2020**, *268*, 127575. [CrossRef]
31. Tasaki, T.; Takase, S.; Shimizu, Y. Improvement of sensing performance of impedancemetric $C_2H_2$ sensor using $SmFeO_3$ thin-films prepared by a polymer precursor method. *Sensors* **2019**, *19*, 773. [CrossRef] [PubMed]
32. Zhang, H.; Xiao, J.; Chen, J.; Zhang, L.; Zhang, Y.; Pei, X. Pd-modified $SmFeO_3$ with hollow tubular structure under light shows extremely high acetone gas sensitivity. *Rare Met.* **2023**, *42*, 545–557. [CrossRef]
33. Han, T.; Ma, S.; Yun, P.; Sheng, H.; Xu, X.; Cao, P.; Pei, S.; Alhadi, A. Synthesis and characterization of Ho-doped $SmFeO_3$ nanofibers with enhanced glycol sensing properties. *Vacuum* **2021**, *191*, 110378. [CrossRef]
34. Zhang, H.; Qin, H.; Zhang, P.; Hu, J. High sensing properties of 3wt% Pd-doped $SmFe_{1-x}Mg_xO_3$ nanocrystalline powders to acetone vapor with ultralow concentrations under light illumination. *ACS Appl. Mater. Interf.* **2018**, *10*, 15558–15564. [CrossRef] [PubMed]
35. Li, L.; Qin, H.; Zhang, L.; Hu, J. Ultrasensitive sensing performances to sub-ppb level acetone for Pd-functionalized $SmFeO_3$ packed powder sensors. *RSC Adv.* **2016**, *6*, 6967–6974.

36. Zhang, H.; Qin, H.; Zhang, P.; Chen, Y.; Hu, J. Low concentration acetone gas sensing properties of 3 wt% Pd-doped $SmCo_xFe_{1-x}O_3$ nanocrystalline powders under UV light illumination. *Sens. Actuators B* **2018**, *260*, 33–41. [CrossRef]
37. Li, K.; Chen, M.; Rong, Q.; Zhu, Z.; Liu, Q.; Zhang, J. High selectivity methanol sensor based on Co-$Fe_2O_3$/$SmFeO_3$ p-n heterojunction composites. *J. Alloys Compd.* **2018**, *765*, 193–200. [CrossRef]
38. Anajafi, Z.; Naseri, M.; Neri, G. Acetone sensing behavior of p-$SmFeO_3$/n-ZnO nanocomposite synthesized by thermal treatment method. *Sens. Actuators B* **2020**, *304*, 127252. [CrossRef]
39. Liu, H.; Cao, Y.; Liu, W.; Chen, J.; Hu, J. Gas response of $SmFeO_3$ planar electrode sensor to volatile organic compounds gases under light illumination. *Mater. Lett.* **2022**, *326*, 133009. [CrossRef]
40. Liu, H.; Miao, T.; Liu, W.; Chen, J.; Cheng, B.; Qin, H.; Hu, J. Highly sensitive acetone gas sensor based on $YFeO_3$ planar electrode under multi-wavelength light illumination. *Mater. Lett.* **2023**, *333*, 133596. [CrossRef]
41. Wang, M.; Wang, T.; Song, S.; Tan, M. Structure-controllable synthesis of multiferroic $YFeO_3$ nanopowders and their optical and magnetic properties. *Materials* **2017**, *10*, 626. [CrossRef]
42. Liu, Y.; Kuo, Y.; Liu, W.; Chou, W. Photoelectrocatalytic activity of perovskite $YFeO_3$/carbon fiber composite electrode under visible light irradiation for organic wastewater treatment. *J. Taiwan Inst. Chem. Eng.* **2021**, *128*, 227–236. [CrossRef]
43. Guo, Y.; Zhang, N.; Huang, H.; Li, Z.; Zou, Z. A novel wide-spectrum response hexagonal $YFeO_3$ photoanode for solar water splitting. *RSC Adv.* **2017**, *7*, 18418–18420. [CrossRef]
44. Zhang, R.; Chen, C.; Jin, K.; Niu, L.; Xing, H.; Luo, B. Dielectric behavior of hexagonal and orthorhombic $YFeO_3$ prepared by modified sol-gel method. *J. Electroceram.* **2014**, *32*, 187–191. [CrossRef]
45. Liu, J.; He, F.; Chen, L.; Qin, X.; Zhao, N.; Huang, Y.; Peng, Y. Novel hexagonal-$YFeO_3$/$\alpha$-$Fe_2O_3$ heterojunction composite nanowires with enhanced visible light photocatalytic activity. *Mater. Lett.* **2016**, *165*, 263–266. [CrossRef]
46. Hu, Q.; Yue, B.; Yang, D.; Zhang, Z.; Wang, Y.; Liu, J. Electrochemical and magnetic properties of electrospun $SmFeO_3$ and $SmCoO_3$ nanofibers. *J. Am. Ceram. Soc.* **2022**, *105*, 1149–1158. [CrossRef]
47. Zhang, Y.; Zou, H.; Peng, J.; Duan, Z.; Ma, M.; Xin, X.; Li, W.; Zheng, X. Enhanced humidity sensing properties of $SmFeO_3$-modified $MoS_2$ nanocomposites based on the synergistic effect. *Sens. Actuators B* **2018**, *272*, 459–467. [CrossRef]
48. Alizadeh, A.; Shariatinia, Z. Unveiling the influence of $SmFeO_3$-$TiO_2$ nanocomposites as high performance photoanodes of dye-sensitized solar cells. *J. Mol. Liq.* **2022**, *348*, 118070. [CrossRef]
49. Nand, M.; Tripathi, S.; Rajput, P.; Kumar, M.; Kumar, Y.; Mandal, S.K.; Urkude, R.; Gupta, M.; Dawar, A.; Ojha, S.; et al. Different polymorphs of Y doped $HfO_2$ epitaxial thin films: Insights into structural, electronic and optical properties. *J. Alloys Compd.* **2022**, *928*, 167099. [CrossRef]
50. Cao, E.; Qin, Y.; Cui, T.; Sun, L.; Hao, W.; Zhang, Y. Influence of Na doping on the magnetic properties of $LaFeO_3$ powders and dielectric properties of $LaFeO_3$ ceramics prepared by citric sol-gel method. *Ceram. Int.* **2017**, *43*, 7922–7928. [CrossRef]
51. Hao, P.; Qu, G.; Song, P.; Yang, Z.; Wang, Q. Synthesis of Ba-doped porous $LaFeO_3$ microspheres with perovskite structure for rapid detection of ethanol gas. *Rare Met.* **2021**, *40*, 1651–1661. [CrossRef]
52. Haryadi, H.; Suprayoga, E.; Suhendi, E. An analysis of electronic properties of $LaFeO_3$ using density functional theory with generalized gradient approximation-perdew-burke-ernzerhof method for ethanol gas sensors. *Mater. Res.* **2022**, *25*, 554. [CrossRef]
53. Cao, Y.; Zhou, C.; Qin, H.; Hu, J. High-performance acetone gas sensor based on ferrite–$DyFeO_3$. *J. Mater. Sci.* **2020**, *55*, 16300–16310. [CrossRef]
54. Ma, L.; Ma, S.Y.; Shen, X.F.; Wang, T.T.; Jiang, X.H.; Chen, Q.; Qiang, Z.; Yang, H.M.; Chen, H. $PrFeO_3$ hollow nanofibers as a highly efficient gas sensor for acetone detection. *Sens. Actuators B* **2018**, *255*, 2546–2554. [CrossRef]
55. Pei, S.; Ma, S.; Xu, X.; Xu, X.; Almamoun, O. Modulated $PrFeO_3$ by doping $Sm^{3+}$ for enhanced acetone sensing properties. *J. Alloys Compd.* **2021**, *856*, 158274. [CrossRef]
56. Lou, Z.; Li, Y.; Zhu, L.; Xie, W.; Niu, W.; Song, H.; Ye, Z.; Zhang, S. The crystalline/amorphous contact in $Cu_2O$/$Ta_2O_5$ heterostructures: Increasing its sunlight-driven overall water splitting efficiency. *J. Mater. Chem. A* **2017**, *5*, 2732–2738. [CrossRef]
57. Bai, S.; Tian, K.; Han, N.; Guo, J.; Luo, R.; Li, D.; Chen, A. A novel rGO-decorated ZnO/$BiVO_4$ heterojunction for the enhancement of $NO_2$ sensing properties. *Inorg. Chem. Front.* **2020**, *7*, 1026–1033. [CrossRef]
58. Bai, S.; Tian, K.; Meng, J.C.; Zhao, Y.; Sun, J.; Zhang, K.; Feng, Y.; Luo, R.; Li, D.; Chen, A. Reduced graphene oxide decorated $SnO_2$/$BiVO_4$ photoanode for photoelectrochemical water splitting. *J. Alloys Compd.* **2021**, *855*, 156780. [CrossRef]